First Constraints on Helium $^+$He^3 Evolution in $z = 3$–4 Using the 8.67 GHz Hyperfine Transition

Cathryn M. Trott[1,2] and Randall B. Wayth[1,2]
[1] International Centre for Radio Astronomy Research, Curtin University, Bentley, Australia
[2] ARC Centre of Excellence for All Sky Astrophysics in 3 Dimensions (ASTRO 3D), Bentley, Australia
Received 2023 August 29; revised 2023 November 16; accepted 2023 November 20; published 2023 December 19

Abstract

We present the first constraints on the cross-correlation power spectrum of the He II ($^+$He^3) signal strength using the redshifted 8.67 GHz hyperfine transition between $z = 2.9$ and 4.1 and with interferometric data obtained from the public archive of the Australia Telescope Compact Array (ATCA). 210 hr of observations of the primary calibrator source B1934-638 were extracted from data obtained with the telescope from 2014–2021, and coherently combined in a power spectrum pipeline to measure the He II power across a range of spatial scales, and at three redshifts that span the period of helium reionization. Our best limit places the fluctuation of the brightness temperature to be less than 557 μK on spatial scales of $30'$ at $z = 2.91$, and less than 755 μK on scales of $30'$ at $z = 4.14$ (2σ noise limited). We measure a temperature of 489 μK at $z = 2.91$. ATCA's few antennas and persistent remaining radio frequency interference in the data prevent deeper integrations improving the results. This work is a proof of principle to demonstrate how this type of experiment can be undertaken to reach the 0.01–$1\,\mu$K level expected for the helium signal at $z \sim 4$.

1. Introduction

The reionization of neutral hydrogen in the first billion years of the Universe (H I→H II) is a major phase transition in the intergalactic medium (IGM), with 75% of the IGM composed of hydrogen gas. This key period is being studied extensively through a number of observational tracers because it traces the formation of the first stars and galaxies (likely responsible for the reionization; Furlanetto et al. 2006). One major observational tracer is the hyperfine transition of neutral hydrogen due to the energy-level splitting from the coupling of the spin states of the proton and electron, with a rest frequency of 1420 MHz (21 cm). The brightness temperature of this line encodes key information about the thermal and radiative state of the IGM, thereby indirectly probing the nature of the first stars and galaxies (Furlanetto et al. 2006; Koopmans et al. 2015). The ionization energy of ground-state hydrogen is 13.6 eV, an energy available to be ionized by photons emitted in the ultraviolet part of the spectrum. The redshifted 21 cm transition is being pursued by many international experiments (Barry et al. 2019; Gehlot et al. 2019; Mertens et al. 2020; Trott et al. 2020; Garsden et al. 2021; HERA Collaboration et al. 2023).

Hydrogen combined at $z \approx 1100$ when the Universe had expanded and cooled sufficiently to bind the electron to the proton. At higher redshifts, $z \approx 6000$, helium recombined (He III → He II), when its inner electron, with a binding energy of 54.4 eV, recombined (Switzer & Hirata 2008). Helium-4 comprises almost 24%, by number, of the IGM after recombination, but helium-3, which has a nonzero magnetic dipole moment that can produce hyperfine splitting, has a substantially smaller abundance (1 part in 10^5, Kneller & Steigman 2004).

The first electron of neutral helium has a similar binding energy as hydrogen and is expected to reionize at similar redshifts to hydrogen ($z > 6$); however, the reionization of singly to doubly ionized helium is expected to occur much later, when active galactic nuclei (AGN) can provide sufficient high-energy photons to unbind the 54.4 eV second electron. This He II to He III process therefore is the second major reionization period of the Universe, liberating further electrons into the IGM. Like hydrogen, the hydrogenic single-electron $^+$He^3 ion has a hyperfine splitting of energy states, emitting an 8.67 GHz photon (3.5 cm, rest).

There is indirect evidence for helium reionization being complete by $z \sim 3$, including optical depth to He II (Worseck et al. 2011, 2016), increased IGM temperature (Lidz et al. 2010; Makan et al. 2021), and hardness of background radiation from metal ionization potentials (Turner et al. 2016; Morrison et al. 2019). Fast radio bursts (FRBs) also have the potential to probe this era because the spectral dispersion of their signals is linearly proportional to the line-of-sight electron component of the IGM (Caleb et al. 2019).

Worseck et al. (2011, 2016) studied the spectra of $z > 3.5$ AGN for evidence of Gunn–Peterson absorption of the helium Lyα forest of the redshifted 304 Å line, reporting that the IGM was highly ionized by $z = 3.4$, due to large transmission regions, and high variance between sightlines. Like the hydrogen Lyα forest, this probe provides detailed information along skewers through the IGM, but is less sensitive to the large-scale signal evolution. Similarly, the large optical depth to the Lyα line (and the saturation of the line at a low neutral fraction) makes this probe sensitive primarily to the end of reionization. McQuinn & Switzer (2010) considered the He I Lyα forest, with a rest wavelength of 584 Å, as a tracer of the reionization of He II. Unlike the He II forest, which saturates easily and has a shorter wavelength, this tracer is weakly absorbed, providing the potential for a quantitative study of singly ionized helium.

Radio observation of the reionization of helium is via the radio hyperfine line, line-of-sight absorption to background AGN (Lyα forest 304 Å line), and indirectly in the IGM electron density (e.g., through observations of the dispersion measure—redshift relation with FRBs and other high-redshift transients). Optical tracers can probe helium-4 because they rely on electron transitions. To date, there has been no detection of the helium-3 hyperfine transition, or attempts to undertake this experiment. Observationally, its small optical depth relative to hydrogen (due primarily to its very small primordial abundance) is balanced somewhat by the lower system temperature and reduced radio foreground at higher frequencies. A number of studies have predicted theoretically (Bagla & Loeb 2009; McQuinn & Switzer 2009), or simulated (Khullar et al. 2020), the helium hyperfine signal in $z = 3$–4, predicting temperature fluctuations spanning 0.1–50 μK on different scales. Khullar et al. (2020) considered the temperature fluctuations of He II around QSOs in simulations at higher redshifts, commensurate with hydrogen reionization.

Detection of intergalactic $^{+}\text{He}^3$ requires a contrast between the resonant signal temperature and the cosmic microwave background (CMB) temperature. McQuinn & Switzer (2009) argue that both weak Wouthysen–Field coupling and small collisional coupling in the IGM would make the temperature contrast small and the signal very difficult to measure. Instead, they consider three avenues for using $^{+}\text{He}^3$ to understand the evolution of the Universe. First, because the absorption of continuum light to a background source by He II is proportional to the source flux density (and not the CMB), identifying and performing spectral absorption measurements on $z > 3.5$ QSOs would be possible. Second, at higher redshift, when He I is transitioning to He II, first producing the 8.67 GHz hyperfine signal, absorption would probe the He I-He II reionization. Finally, He II that is self-shielded in halos with sufficient density for collisional coupling to produce an emission signal could be used to trace the biased signal evolution (similar to post-reionization hydrogen).

In this paper, we aim to place constraints on the spherically averaged (three-dimensional) power spectrum of brightness temperature fluctuations of singly ionized helium-3 over $z = 2.9$–4.2. This work acts as a demonstration of how to undertake this experiment with real telescope data. In Section 2, we introduce the methods, including theoretical predictions and observations; in Section 2.3, the power spectrum methodology is introduced; in Section 3, the results are presented, before being discussed in Section 4.

2. Methods

2.1. Theoretical Predictions and Observational Approaches

The optical depth to $^3\text{He}^+$ is given by McQuinn & Switzer (2009) as

$$\tau_{\text{He}^+} = \frac{c^3 \hbar A_{10}}{16 k_B T_s \nu_{10}^2} \frac{n_{^3\text{He}^+}}{(1 + z) dv/dy}, \tag{1}$$

where A_{10} is the spontaneous emission rate, $\nu_{10} = 8666$ MHz is the rest frequency, $n_{^3\text{He}^+}$ is the helium-3 gas density, which is computed as a fractional abundance of the hydrogen density (1.04×10^{-5}), and dv/dy is the proper velocity per unit conformal distance. Although the helium fraction to hydrogen is small, the spontaneous emission rate is 670 times larger, offsetting some of the reduction. The spin temperature, T_s, is

set by the relative occupancy of the two energy states, and like hydrogen, is set by the thermal, collisional, and radiative properties of the medium. The differential brightness temperature of the emission (temperature relative to the CMB), is then given by Furlanetto et al. (2006) and Bagla & Loeb (2009) as

$$\delta T_b \simeq 18 \, \mu\text{K} \, x_{\text{He II}} \left(1 - \frac{T_{\text{CMB}}}{T_s} \right) \left(\frac{1 + \delta}{10} \right) \left(\frac{1 + z}{9} \right)^2$$
$$\times \left(\frac{n_{3,\text{He}}/n_\text{H}}{1.1 \times 10^{-5}} \right) \left[\frac{H(z)}{(1 + z)(dv_\parallel/dr_\parallel)} \right]. \tag{2}$$

During hydrogen reionization ($z = 6$–10), brightness temperature fluctuations in helium-3 are driven by spin temperature coupling to the gas temperature. Bagla & Loeb (2009) suggest that helium fluctuations at the time of hydrogen reionization are driven by density inhomogeneities and coupling to the gas kinetic temperature, which can be 10^4 K in ionized regions. In the hydrogen post-reionization era, they propose that high-energy photons from AGN can reionize helium-3, and that brightness temperature fluctuations will be dominated by ionization status and gas kinetic temperature inhomogeneities.

Equation (2) shows that a nonzero emission signal relies on $T_{\text{CMB}} \neq T_s$. At $z = 3.6$, McQuinn & Switzer (2009) argue that the low collisional coupling in the IGM and weak radiative spin coupling prevents T_s from coupling to the gas kinetic temperature and instead keeps it coupled to the CMB temperature. Observation of emission signal is therefore only feasible for He II that is self-shielded from reionization in halos, where the density is such for collisional coupling to increase the spin temperature. These overdense regions ($\Delta_b \gtrsim 100$, $n_e \gtrsim 3 \times 10^{-6} \text{cm}^{-3}$) may comprise $X = 1\%$–10% of the gas mass density. In IllustrisTNG simulations, Martizzi et al. (2019) found that 1%–15% of gas resided at these densities from $z = 4$–2. In this scenario, the helium signal traces the halo distribution with an order-unity bias, b, giving a nominal power of

$$P(k) \simeq \left(18 \, \mu\text{K} \left(\frac{1 + \delta}{10} \right) \left(\frac{1 + z}{9} \right)^2 \right)^2 X^2 b^2 P_m(k)$$
$$= (0.6 \, \mu\text{K})^2 X^2 b^2 P_m(k) \, h^{-3} \text{Mpc}^3, \tag{3}$$

where $P_m(k)$ is the matter power spectrum, and we have assumed $z = 4$ and $\delta = 0$. We use the CAMB software[3] (Lewis & Bridle 2002; Lewis 2013), to generate the matter power spectrum between $z = 2.9$ and 4.1.

At $z \simeq 3 - 4$, the redshifted hyperfine line is observed at 1700–2200 MHz, in contrast to hydrogen's 21 cm line being redshifted to 100–200 MHz. Observationally, the sky temperature at higher frequencies (which dominates the system temperature at low frequencies), is substantially lower, yielding lower radiometric noise ($T \propto \nu^{-2.6}$). Other key factors in determining the utility of observations are the field of view (FOV) ($\propto \lambda$), the instantaneous bandwidth (for continuum foreground fitting and removal) and spectral resolution (for matching ionization regions), and the amplitude of ionospheric refraction ($\propto \lambda^2$).

Simulations of Compostella et al. (2013) and McQuinn et al. (2009) show that IGM kinetic temperature and ionization

---

[3] https://camb.info/

fraction fluctuations can be observed on spatial scales of 1–50 cMpc at $z = 3.5$, corresponding to $1'$–$20'$ angular scales and 1–30 MHz spectral scales from an observational standpoint. Any experiment to attempt the intergalactic signal would be suited to an array with baselines of $x = u\lambda = \lambda/\Delta\theta \simeq 30$–500 m (at $\lambda = 17$ cm), and a dish aperture of $d = \lambda/\text{FOV} < 30$ m. These parameters are well matched to the Australia Telescope Compact Array (ATCA), and provide the starting point for our analysis.

2.2. Observations

The ACTA[4] is a six-element dish-based interferometer that is mostly operated in an east–west configuration, at the Paul Wild Observatory near Narrabri NSW. Each dish has a diameter of 22 m, and is fed by multiple interchangeable feeds, operating at centimeter and millimeter wavelengths. The CABB backend, installed in 2009, allows for an instantaneous 2048 MHz of bandwidth (Wilson et al. 2011). For our experiment, we limit data to those observed in the 1.1–3.1 GHz CABB band, with 1 MHz spectral resolution over 2048 channels. The ATCA operates in a number of array configurations. For this work, the archive was searched for all 6 km, 1.5 km, and 750 m configurations, with array minimum and maximum baselines spanning 30.6–6000 m. The shorter of these baselines, and the spectral resolution and bandwidth of the CABB, are well suited for an interferometric helium experiment. What is less well suited, is the low sensitivity afforded by the small number of antennas. With the sixth antenna (fixed at a minimum baseline of 3 km from the others) effectively unusable for this science, there are only 10 baselines available for integration. This will limit the sensitivity of the experiment compared with another array with better uv-coverage and sensitivity.

Due to the low sensitivity of the ATCA, and the desire to undertake a proof-of-principle experiment, we chose to use public data from the extensive ATCA archive, rather than propose new multi-year observations. To undertake a coherent experiment (where the noise can be reduced most effectively by observing the same patch of sky for the full observation), a field is required where the ATCA has spent substantial observing time, and preferably with a simple foreground source that can be easily removed. The primary calibrator source, B1934-638, fits both of these criteria: it has been one of the most-observed calibrator sources for data over the lifetime of the CABB, and it is a well-modeled unresolved source, with a single power-law spectrum, and a flux density of ∼12 Jy at 1500 MHz.

The ATCA archive[5] was searched for observations containing source B1934-638, using the CABB backend over 1.1–3.1 GHz with 1 MHz spectral resolution, for all 6 km, 1.5 km, and 750 m baseline configurations, and dates spanning 2014–2022 (public data). These individual observations were inspected manually to extract those with >30 minutes of continuous observation of the source. This provided a set of longer observations to reduce the number of observations to be flagged. The search yielded 410 hr of data.

2.3. Data Analysis

We used the data reduction software MIRIAD (Sault et al. 1995) to flag and calibrate data for further analysis. The CABB

---

backend outputs data across two intermediate frequencies. For the data used in this project, the channels were listed in reverse order (decreasing frequency). After visual inspection of a few data sets using uvspec, it was clear that there were bands of persistent radio frequency interference (RFI) that affected all CABB data. These were flagged across all data sets using UVFLAG. In addition, the top and bottom of the band were flagged due to large regions of RFI, and the desire to analyze data outside of the local 21 cm band (1420 MHz) and below 2.2 GHz. The first 400, and final 827 channels were flagged, leaving 650 channels spanning 1676–2325 MHz ($z = 4.2$–2.7). Each data set was then manually inspected using UVSPEC, with auto- and cross-correlations visualized after averaging each 60 minutes of data. RFI identified by visual inspection were manually flagged using UVFLAG. In addition, poorly performing baselines or antennas were also flagged. After the first round of flagging, data were calibrated using MFCAL. Because B1934-638 is the primary calibrator for ATCA, no other field data were required. After calibration, data sets were inspected again with UVSPEC. All data that appeared RFI-free and showed cross-correlations consistent with expectations (flat ∼12 Jy continuum source) were retained for further analysis. After the rejection of poorly calibrated observations, there were 210 hr of data.

The foreground source, B1934-638, is well fitted by a first-order polynomial. Fitting across the full 650 MHz does not affect the helium-3 structures of interest in this work, due to the very broad backend. First-order fits were subtracted from the visibilities using the uvlin procedure. Residual data and weights were written to UVFITS format using the MIRIAD FITS procedure for the XX and YY polarizations, and all baselines, with a temporal and spectral resolution of 10 s and 1 MHz, respectively.

2.4. Power Spectrum Estimation

For hydrogen reionization, there are many power spectrum estimation pipelines available. For the Murchison Widefield Array Epoch of Reionization project, we employ the CHIPS software to estimate the spherically averaged power spectrum (Trott et al. 2016). CHIPS natively reads the UVFITS files produced by MIRIAD. We adjusted the software to create CHeIIPS, a package that uses the same methodology but with parameters updated to match that for the helium-3 reionization experiment (e.g., gridding kernel size, uv-plane resolution).

Full details of the methodology are available in Trott et al. (2016), and are briefly reproduced here. Channelized calibrated visibilities are cumulatively gridded onto a three-dimensional uv-plane grid (u, v, ν) as complex doubles, along with a separate weights grid that accumulates the gridding kernel. The kernel would optimally be set to the Fourier transform of the telescope primary beam; for CHIPS and CHeIIPS, a matched-size 2D Blackman–Harris window is employed due to its better sidelobe suppression performance. In Trott et al. (2016), this choice was shown to not produce signal loss. Data are split into two data sets, interleaved in time, where each consecutive 10 s timestep is assigned alternately to even and odd grids. This allows for the data cross-power spectrum to be computed, whereby noise power that would be present due to the squaring of a quantity is absent (noise being uncorrelated between time steps). This choice comes at the expense of slightly higher noise uncertainty.

Table 1
Starting Frequencies, Central Redshift, and Number of Spectral Channels for each Sub-band Selected from the Data

ν_{low} (MHz)	z_{cent}	N_{ch}
1676	4.17	60
1686	*4.14*	*80*
1781	3.86	54
1902	3.55	96
1933	3.48	96
1974	*3.39*	*54*
2110	3.10	42
2216	*2.91*	*60*

Note. The italicized sub-bands were used in the final analysis.

In the first stage of analysis, data were coherently gridded into 20 sets of 10 hr each. This allowed for the inspection of individual sets of power spectra to identify any poorly behaved observations that had passed calibration assessment. After coherent gridding, the data were normalized by the weights to produce the averaged gridded data:

$$\tilde{V}(u, v, \nu) = \frac{\sum_i V_i W_i}{\sum_i W_i}, \quad (4)$$

where W_i is the visibility weight multiplied by the gridding kernel.

The final frequency transform to Fourier space ($\nu - \eta$) is performed for each uv-cell. For CHIPS, where the residual foregrounds are bright and complex, a Blackman–Harris window function is employed to reduce foreground sidelobe contamination. This is undertaken at the cost of a broader main lobe in η space. For these helium-3 data, the foreground source has been effectively removed by fitting the first-order polynomial, and no spectral window function is required.

After spectral transform via a discrete Fourier transform, the final (u, v, η) data and weights cubes were used for power spectrum analysis. Transform across the full 650 MHz is not appropriate because the signal evolves and is not ergodic. In addition, the many missing spectral channels due to flagging of persistent RFI leave gaps in the data that produce very poor power spectral results. As such, we choose bands of gridded data that contain no missing data, and limit the line-of-sight transform to a maximum of 100 MHz ($\Delta z \simeq 0.25$). Eight overlapping sub-bands were identified that met these criteria. These are described in Table 1.

Cylindrically and spherically averaged power spectra are produced by squaring the gridded, transformed visibilities and incoherently averaging them using the gridded weight data. The cylindrical transform plots angular ($k_\perp = \sqrt{k_x^2 + k_y^2}$, $k_x \propto u$) and line-of-sight ($k_\parallel \propto \eta$) modes separately:

$$P(k_\perp, k_\parallel) = \frac{\sum_{i \in k} V_i^* V_i W_i^2}{\sum_{i \in k} W_i^2} \; \text{Jy}^2\text{Hz}^2, \quad (5)$$

where W_i is the summed weights over all frequency channels. The power is transformed from observational units of $\text{Jy}^2 \, \text{Hz}^2$ to cosmological units of $\text{mK}^2 \, \text{h}^{-3} \, \text{Mpc}^3$ using standard
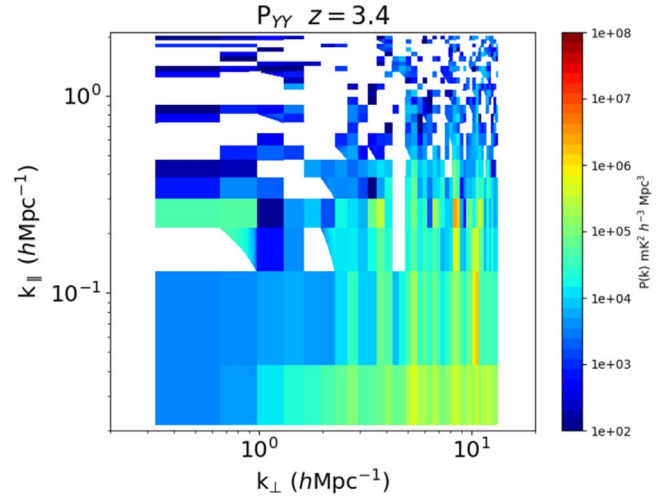

Figure 1. Cylindrically averaged power spectrum at $z = 3.4$ over 54 MHz of bandwidth, and the YY polarization. Missing data denote negative cross-power, highlighting noise-like regions. This figure has units of $\text{mK}^2 \, \text{h}^{-3} \, \text{Mpc}^3$.

transforms and the transverse comoving distance at the sub-band centers. Finally, the dimensionless power spectrum is computed as

$$\Delta^2(k) = \frac{k^3 P(k)}{2\pi^2} \, \mu\text{K}^2, \quad (6)$$

where a final conversion from milli-Kelvin to micro-Kelvin is performed. In one dimension, we display the square root of this quantity, equivalent to the spectrum of temperature fluctuations.

3. Results

The 2D and 1D power spectra were inspected for each subset of 10 hr of observations, for each sub-band described in Table 1. Most subsets displayed reasonable results, where the power was consistent with thermal noise across most wavemodes. One subset showed clear systematic contamination and was removed from the final coherent average. The remaining subsets were coherently averaged to $\simeq 190$ hr of data, except for the $z = 4.14$ sub-band, where only 120 hr of data showed good behavior.

The eight individual sub-bands showed different systematic behavior. Three that spanned the full band displayed the cleanest data, with most modes consistent with thermal noise. These sub-bands are italicized in Table 1, and correspond to power at $z = 2.91$, 3.39, and 4.14. These were processed to the final power spectra. Figure 1 displays a 2D power spectrum at $z = 3.39$ in units of $\text{mK}^2 \, \text{h}^{-3} \, \text{Mpc}^3$. The DC ($k_\parallel = 0$) mode has been omitted. The data show positive and negative modes, consistent with thermal noise when cross-power spectra are considered. The positive modes at high $k_\perp$ and low $k_\parallel$ show residual foreground power that has not been removed by the linear fitting to the visibilities.

The three sub-bands of data are then spherically averaged to 1D, for each polarization, and square rooted to produce the spectrum of temperature fluctuations shown in Figure 2. In each, the blue-shaded region denotes the 2σ thermal noise with noise-dominated regions showing shading to the bottom of the plot. The red points and blue lines denote the measured power,
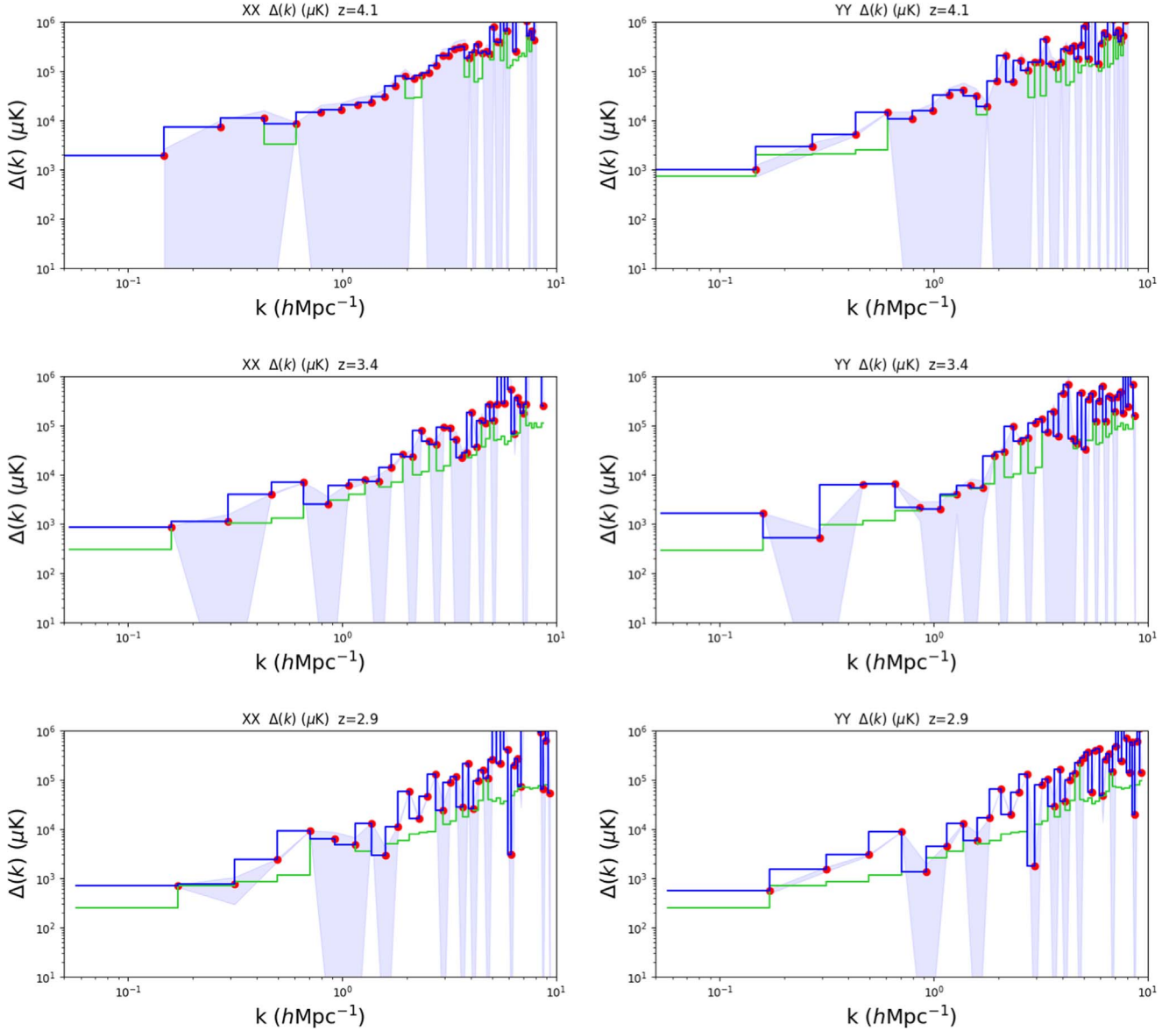
Figure 2. Spherically averaged temperature fluctuation (μK) as a function of wavenumber for $z = 4.1$, 3.4, and 2.9 (top to bottom) across 80 MHz of bandwidth and the XX (left) and YY (right) polarizations. The blue-shaded region denotes the 2σ thermal noise with noise-dominated regions showing shading to the bottom of the plot. The red points and blue lines denote the measured power, while the green lines denote the estimated 2σ noise level.

while the green lines denote the estimated 2σ noise level. Many modes are consistent with thermal noise. The best measured temperature is at $z = 2.91$ with $\Delta(k) = 489 \mu$K, and a 2σ upper limit of 557 μK. Table 2 displays the measured and upper limit temperature fluctuations for the three sub-bands and their angular scale. For all redshifts, the YY power spectrum yielded cleaner results, and are reported here. The XX polarization results are only marginally poorer, and this likely points to localized RFI that affects one polarization more than the other. In each case, the angular mode corresponds to the shortest baseline available to the ATCA (30.6 m), which is typically occupied by a single baseline, and therefore has poor sensitivity. For comparison, Figure 3 shows the expected temperature fluctuation of the shielded model from Equation (3), for $z = 2.9$ and 4.1, and assuming that 10% of gas is collisionally coupled. The broad level is $\sim$0.01–0.1 μK, which is 3–4 orders of magnitude below the measurements, demonstrating the difficulty of the experiment.

Table 2
Measured Temperature and 2σ Upper Limits for Each of the Three Sub-bands and the YY Polarization, and the Angular Mode of the Lowest Temperature

z_{cent}	Meas. $\Delta(k)$ μK	2σ limit	k (h^{-1} Mpc)	$\Delta\theta$ (')
4.14	534	757	0.15	29
3.39	689	760	0.16	29
2.91	489	557	0.17	29

4. Discussion

This work is an attempt to place upper limits on the power spectrum of temperature fluctuations for helium-3, and provides an approach to how to undertake such an experiment. Despite not having the sensitivity to theoretically detect the signal, our data exhibit two important characteristics that currently impede interferometric 21 cm experiments pursuing hydrogen reionization: (1) a single clean and simple foreground
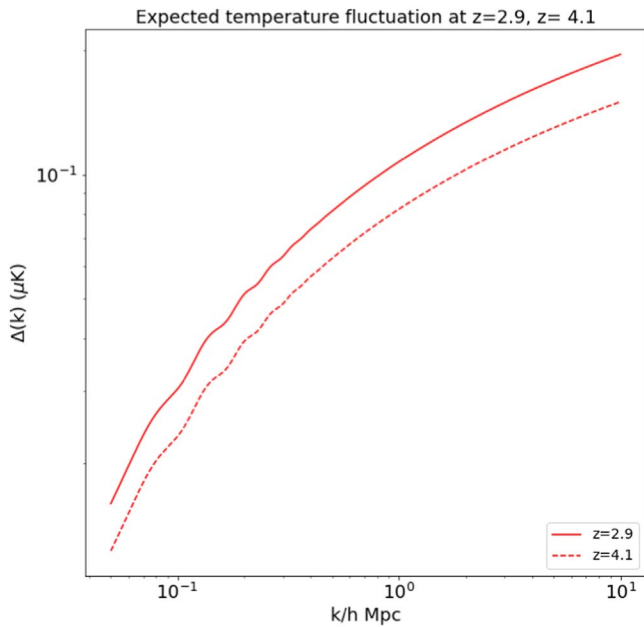
Figure 3. The expected temperature fluctuation of the shielded model from Equation (3), for $z = 2.9$ and 4.1, while assuming that 10% of gas is collisionally coupled.

Figure 4. Spherically averaged temperature fluctuation (μK) as a function of wavenumber for $z = 3.6$ across 96 MHz of bandwidth and the YY polarization. These data are affected by residual spectral structure from RFI or the foreground fitting leading to poor performance at low k.

source that can be removed effectively, due to the wide instantaneous bandwidth; and (2) sufficiently low residual RFI that the data are mostly noise limited at 200 hr.

The accuracy of the subtraction of B1934-638 is sufficient at the 200 hr level, but there are indications that both a first- and second-order polynomial fit leaves residuals that are not consistent with zero-mean noise in some parts of the band. The residual signal in a 1 MHz channel should not exceed 1 μJy, according to McQuinn & Switzer (2009), requiring a dynamic range of 10^7 for a 12 Jy source. If the source can be fitted by a low-order polynomial, then the full band can be used for foreground estimation and subtraction, providing a sufficient signal-to-noise ratio, e.g., across 650 channels and fitting for a single parameter, 200 hr with all 15 ATCA baselines yields a dynamic range of 2×10^6. Increasing the order of the polynomial fit increases the chances of signal loss, by introducing a spectral structure that has a nonzero projection onto the spectral helium-3 structure (i.e., the complex spectral structure may be due to helium-3, and not the foreground source), whereas a first-order polynomial over 650 MHz will not impact the underlying helium-3 structure (any global helium-3 signal evolution has already been removed by omitting the autocorrelations).

Residual RFI and spectral structure do affect a lot of the band; hence, is why only three out of the eight bands were used for the final analysis. Figure 4 displays YY power spectra for a poorly performing sub-band of 96 channels near $z = 3.6$. For these data, there is residual spectral structure across the sub-band visible in the gridded visibility spectra, leading to increased leakage from foreground modes.

It may be noted that the autocorrelation data may be used to study the evolution of the global temperature of the helium-3 signal. With a single power-law continuum source as the only bright foreground in the field, a broad non-power-law evolution of the spectrum may indicate the global reionization of helium (similar to that undertaken with the EDGES experiment for hydrogen; Bowman et al. 2018). However, an inspection of the
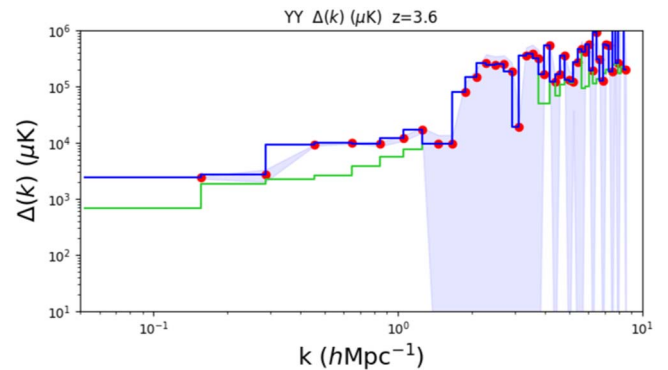
autocorrelations from ATCA show high-amplitude oscillations, consistent with reflections off structures within the dishes. The systematics in these data were not deemed able to be modeled sufficiently to undertake this experiment. Similarly, one may perform a helium-3 absorption study with the cross-correlation spectra, *if* B1934-638 were a background, high-redshift source (instead, it is $z = 0.12$). McQuinn & Switzer (2009) predicted that absorption against a background continuum source provided the highest detectability because the absorption flux density is dictated by the strength of the source and the optical depth. Given the lack of expected emission signal from the IGM, and the low signal expectation from the self-shielded gas in halos, the absorption study may be the best observational approach to tackle.

ATCA is well suited to undertake this experiment, due to its wide CABB backend and small field of view, but is ultimately hampered by its few baselines and lack of sensitivity. Prospects for detection with other current and future telescopes are dependent on (1) overall sensitivity; (2) FOV (too small and the results are sample variance limited and too large and the foregrounds become complicated); (3) low-RFI environment to retain spectral smoothness and afford bands without flagged channels; (4) short baselines to access large-scale structures; and (5) a broad, instantaneous bandwidth to measure the full signal evolution and for accurate foreground removal. Few telescopes have all of these properties, in particular, the wideband backend system.

The Square Kilometre Array (SKA)-Mid is an obvious instrument for this experiment. Band 3, which is not proposed to be available initially[6], spans 1400 MHz instantaneously across 1650–3050 MHz. Bands 1 and 2 would probe helium at higher redshift. Using the SKA-Mid baseline distribution (Braun et al. 2019), there will be $\simeq$90 baselines with physical lengths shorter than 50 m. With this configuration, a 100 hr, 100 MHz bandwidth experiment should yield noise levels of 1 μK at $k = 0.14\,h\,\text{Mpc}^{-1}$, in the absence of RFI and other spectral systematics. The precursor MeerKAT array has $\simeq$10 baselines shorter than 50 m (minimum 29 m), and with an existing wideband S-band receiver, should reach $1 \simeq \mu$K noise level after 1000 hr. Other facilities with good *uv*-coverage have narrower fractional bandwidth at these frequencies, which will hinder their ability to perform accurate foreground subtraction without the potential for signal loss (e.g., the Very Large

---

6 http://www.skao.int

Array). Higher-redshift $^+\mathrm{He}^3$, as explored by Khullar et al. (2020), is accessible at lower frequencies, but there are few radio interferometers with feeds that access 800–1200 MHz. For gas around $z = 5.1$ (1420 MHz), the signal will be confused with local neutral hydrogen, making its observation almost impossible.

5. Conclusions

We attempted a measurement of the spherically averaged power spectrum of $^+\mathrm{He}^3$ (single-ionized helium-3) using the 3.5 cm (8.67 GHz) hyperfine line, at $z = 2.9$–4.1 using 190 hr of publicly available data from the ATCA archive. After RFI flagging, identification of spectral bands with no missing data, and a simple foreground subtraction, power spectra were found to be noise limited across many angular wavemodes. The upper limits on the power are not cosmologically interesting, being 3–4 orders of magnitude larger in temperature than theoretical expectations, but is the first attempt to measure this signal. This work demonstrates the potential for this experiment to yield improved results, which would be cosmologically relevant, with a telescope with higher sensitivity.

Acknowledgments

Facility: Australia Telescope Compact Array.

Software: MIRIAD, https://www.atnf.csiro.au/computing/software/miriad/ (Sault et al. 1995).

ORCID iDs

Cathryn M. Trott https://orcid.org/0000-0001-6324-1766
Randall B. Wayth https://orcid.org/0000-0002-6995-4131

References

Bagla, J. S., & Loeb, A. 2009, arXiv:0905.1698
Barry, N., Wilensky, M., Trott, C. M., et al. 2019, ApJ, 884, 1
Bowman, J. D., Rogers, A. E. E., Monsalve, R. A., Mozdzen, T. J., & Mahesh, N. 2018, Natur, 555, 67
Braun, R., Bonaldi, A., Bourke, T., Keane, E., & Wagg, J. 2019, arXiv:1912.12699
Caleb, M., Flynn, C., & Stappers, B. W. 2019, MNRAS, 485, 2281
Compostella, M., Cantalupo, S., & Porciani, C. 2013, MNRAS, 435, 3169
Furlanetto, S. R., Oh, S. P., & Briggs, F. H. 2006, PhR, 433, 181
Garsden, H., Greenhill, L., Bernardi, G., et al. 2021, MNRAS, 506, 5802
Gehlot, B. K., Mertens, F. G., Koopmans, L. V. E., et al. 2019, MNRAS, 488, 4271
HERA Collaboration, Abdurashidova, Z., Adams, T., et al. 2023, ApJ, 945, 124
Khullar, S., Ma, Q., Busch, P., et al. 2020, MNRAS, 497, 572
Kneller, J. P., & Steigman, G. 2004, NJPh, 6, 117
Koopmans, L., Pritchard, J., Mellema, G., et al. 2015, in Advancing Astrophysics with the Square Kilometre Array (AASKA14) (Trieste: Sissa), 1
Lewis, A. 2013, PhRvD, 87, 103529
Lewis, A., & Bridle, S. 2002, PhRvD, 66, 103511
Lidz, A., Faucher-Giguère, C.-A., Dall'Aglio, A., et al. 2010, ApJ, 718, 199
Makan, K., Worseck, G., Davies, F. B., et al. 2021, ApJ, 912, 38
Martizzi, D., Vogelsberger, M., Artale, M. C., et al. 2019, MNRAS, 486, 3766
McQuinn, M., Lidz, A., Zaldarriaga, M., et al. 2009, ApJ, 694, 842
McQuinn, M., & Switzer, E. R. 2009, PhRvD, 80, 063010
McQuinn, M., & Switzer, E. R. 2010, MNRAS, 408, 1945
Mertens, F. G., Mevius, M., Koopmans, L. V. E., et al. 2020, MNRAS, 493, 1662
Morrison, S., Pieri, M. M., Syphers, D., & Kim, T.-S. 2019, MNRAS, 489, 868
Sault, R. J., Teuben, P. J., & Wright, M. C. H. 1995, in ASP Conf. Ser. 77, Astronomical Data Analysis Software and Systems IV, ed. R. A. Shaw, H. E. Payne, & J. J. E. Hayes (San Francisco, CA: ASP), 433
Switzer, E. R., & Hirata, C. M. 2008, PhRvD, 77, 083006
Trott, C. M., Jordan, C. H., Midgley, S., et al. 2020, MNRAS, 493, 4711
Trott, C. M., Pindor, B., Procopio, P., et al. 2016, ApJ, 818, 139
Turner, M. L., Schaye, J., Crain, R. A., Theuns, T., & Wendt, M. 2016, MNRAS, 462, 2440
Wilson, W. E., Ferris, R. H., Axtens, P., et al. 2011, MNRAS, 416, 832
Worseck, G., Prochaska, J. X., Hennawi, J. F., & McQuinn, M. 2016, ApJ, 825, 144
Worseck, G., Prochaska, J. X., McQuinn, M., et al. 2011, ApJL, 733, L24